

Supporting Information

Single Atom and Bimetallic Nano-alloy Supported on Nanotubes as a Bifunctional Electrocatalyst for Ultrahigh Current Density Overall Water Splitting

*Wenhui Luo^a, Yang Wang^a, Liuxiong Luo^b, Shen Gong^{*a}, Mengni Wei^b, Yixuan Li^b,*

*Xueping Gan^{*a}, Yuyuan Zhao^b, Zhenghong Zhu^c and Zhou Li^{*a}*

a Dr. W. H. Luo, Dr. Y. Wang, L. X. Luo, Prof. S. Gong, M. N. Wei, Y. X. Li, Prof. X. P. Gan, Prof. Z. Li

State Key Laboratory of Powder Metallurgy

School of Materials Science and Engineering

Central South University

Changsha, 410083, P. R. China

E-mail: gongshen011@csu.edu.cn; ganxueping@csu.edu.cn; lizhou6931@csu.edu.cn

b Prof. Y. Y. Zhao

School of Engineering

University of Liverpool

Liverpool, L69 3GH, UK

c Prof. Z. H. Zhu

Department of Mechanical Engineering

York University

Toronto, M3J 1P3, Canada

Glassy carbon electrode preparation:

The preparation process of electrode is similar to that of carbon cloth electrode. 3.0mg of catalysts were dispersed in a mixed solution containing 400 μ L ethanol and 20 μ L 5% Nafion solution and then sonicated for 2h. Subsequently, 5 μ L of catalyst ink was dropped on glassy carbon electrode (effective working area, 0.071 cm⁻²) and dried at room temperature.

Supplementary figures

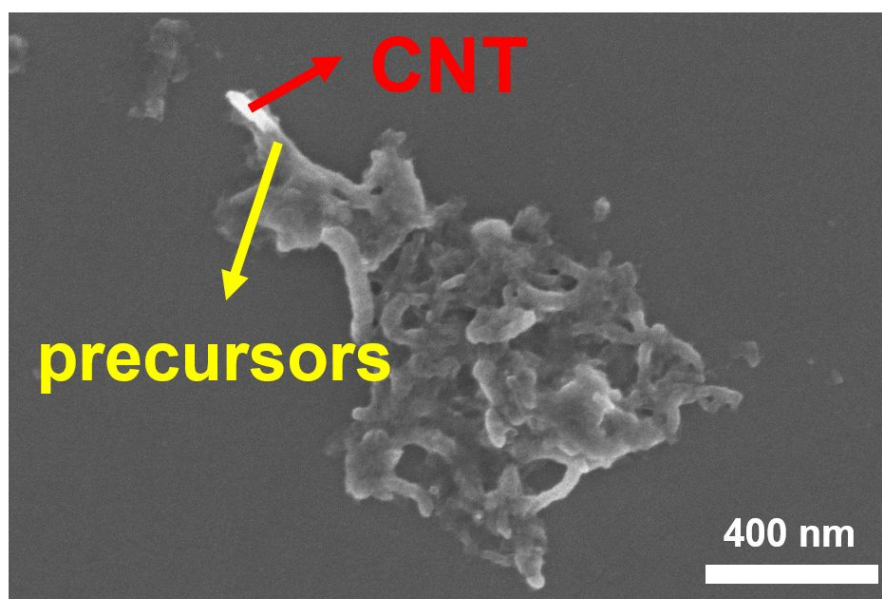


Figure S1. SEM image of precursors/CNT.

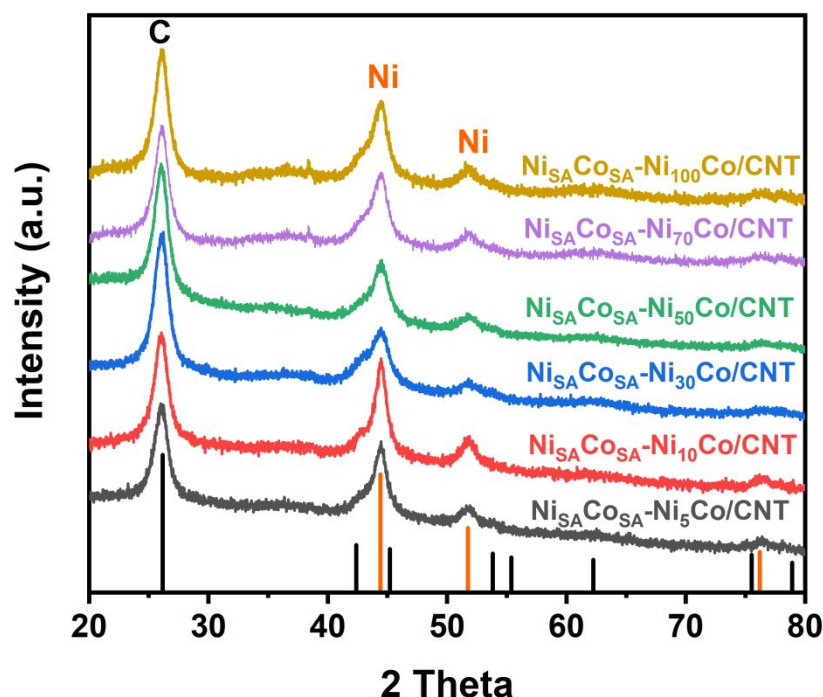


Figure S2. XRD patterns of $\text{Ni}_{\text{SA}}\text{Co}_{\text{SA}}\text{-Ni}_x\text{Co/CNT}$.

Figure S2 shows the XRD diffraction patterns of $\text{Ni}_{\text{SA}}\text{Co}_{\text{SA}}\text{-Ni}_x\text{Co/CNT}$. It can be seen from the figure that the diffraction peaks of $\text{Ni}_{\text{SA}}\text{Co}_{\text{SA}}\text{-Ni}_5\text{Co/CNT}$, $\text{Ni}_{\text{SA}}\text{Co}_{\text{SA}}\text{-Ni}_{10}\text{Co/CNT}$, $\text{Ni}_{\text{SA}}\text{Co}_{\text{SA}}\text{-Ni}_{30}\text{Co/CNT}$, $\text{Ni}_{\text{SA}}\text{Co}_{\text{SA}}\text{-Ni}_{50}\text{Co/CNT}$ and $\text{Ni}_{\text{SA}}\text{Co}_{\text{SA}}\text{-Ni}_{100}\text{Co/CNT}$ are almost the same, which can match to C and Ni. The radius of Ni and Co atoms are close to each other, so the diffraction peaks will not shift obviously after forming the alloy. In addition, it can be seen from the figure that the diffraction peak intensity of the alloy is lower than that of the C peak, indicating that the size of the alloy particles is small.

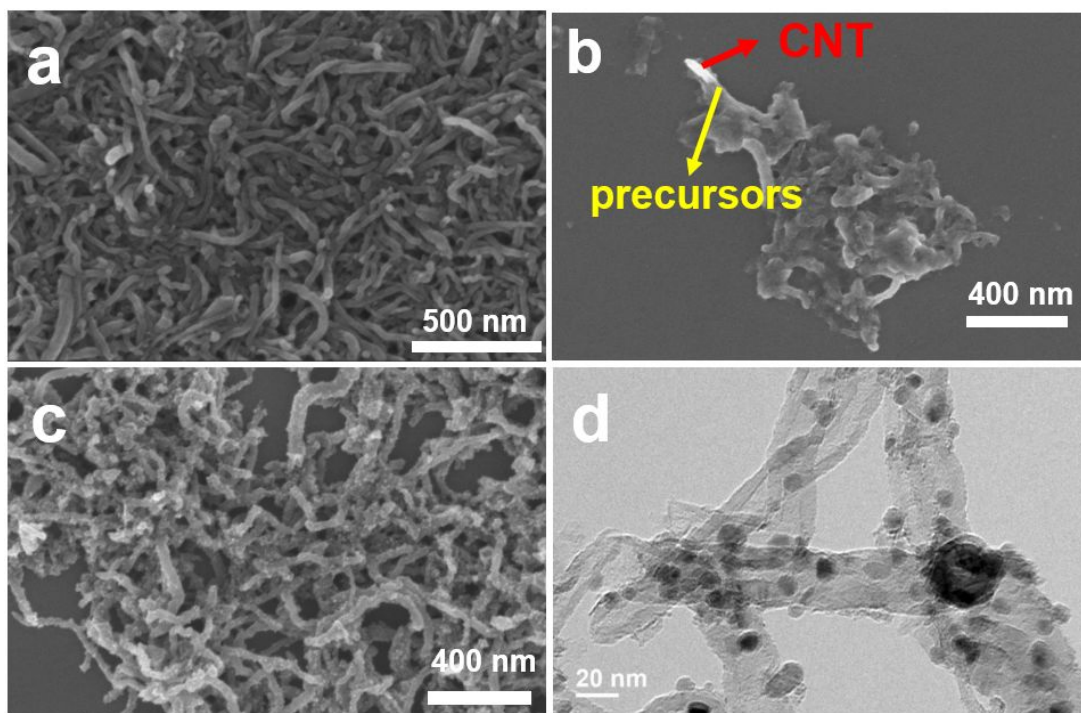


Figure S3. a) SEM image of CNT after acid treatment. b) SEM image of $\text{Ni}_{\text{SA}}\text{Fe}_{\text{SA}}\text{-Ni}_{50}\text{Fe/CNT}$ precursor reduced by NaBH_4 . c) SEM image of $\text{Ni}_{\text{SA}}\text{Co}_{\text{SA}}\text{-Ni}_{10}\text{Co/CNT}$. d) TEM image of $\text{Ni}_{\text{SA}}\text{Co}_{\text{SA}}\text{-Ni}_{10}\text{Co/CNT}$.

Figure S3a and **b** show the SEM images of CNT after acid treatment and precursor/CNT after NaBH_4 reduction, respectively. The low concentration of the reducing agent provides a reducing environment, which makes Ni^{2+} , Fe^{3+} , Co^{2+} and PVP adsorb on the defects of CNT and form small nucleation sites. The SEM and TEM images of $\text{Ni}_{\text{SA}}\text{Co}_{\text{SA}}\text{-Ni}_{10}\text{Co/CNT}$ are shown in **Figure S3c** and **d**, respectively. It can be seen from the figures that the size of Ni_{10}Co alloy nanoparticles is uniform, and the size is about 10nm.

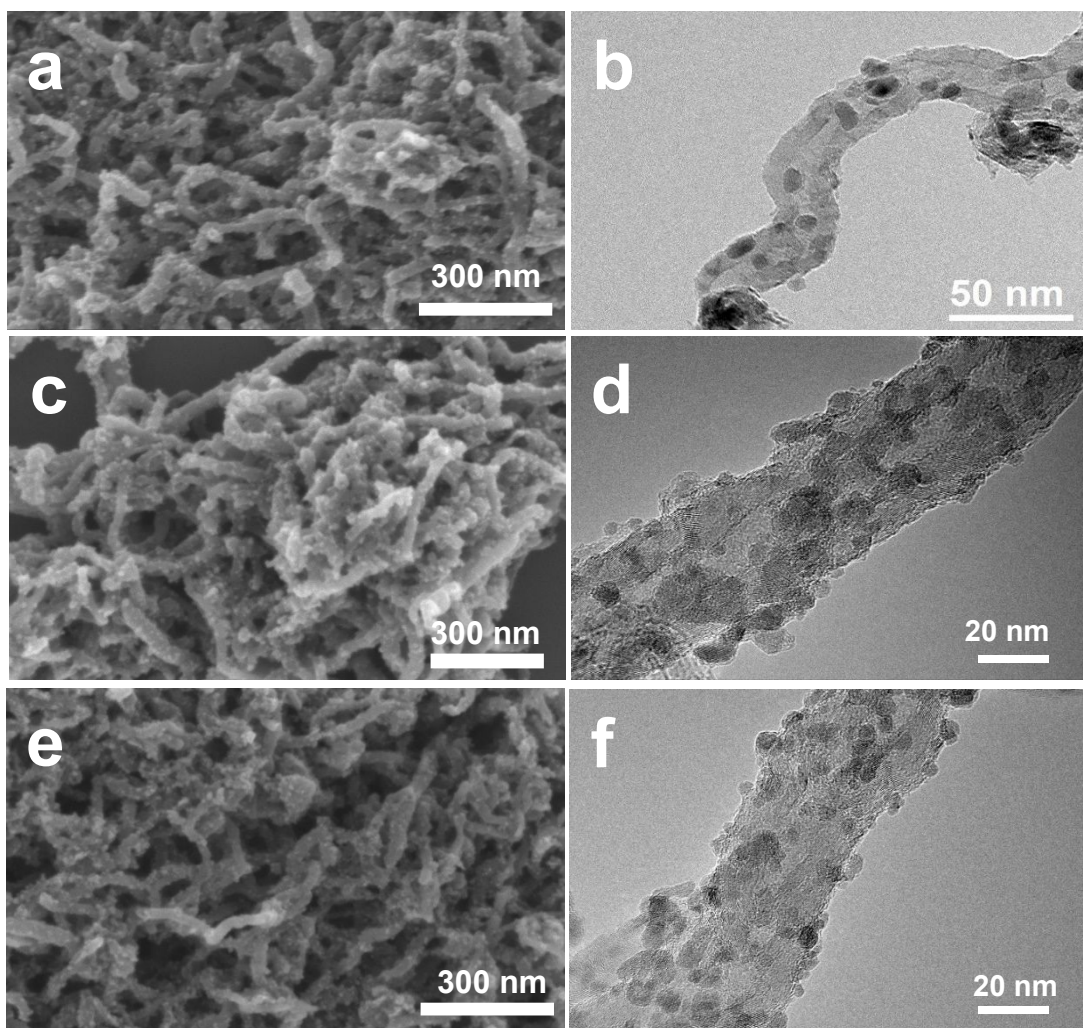


Figure S4. a) SEM image of Ni_{SA}-Ni/CNT. b) TEM image of Ni_{SA}-Ni/CNT. c) SEM image of Ni_{SA}Fe_{SA}-Ni₅Fe/CNT. d) TEM image of Ni_{SA}Fe_{SA}-Ni₅Fe/CNT. e) SEM image of Ni_{SA}Co_{SA}-Ni₅Co/CNT. f) TEM image of Ni_{SA}Co_{SA}-Ni₅Co/CNT.

The SEM and TEM images of Ni_{SA}-Ni/CNT, Ni_{SA}Fe_{SA}-Ni₅Fe/CNT and Ni_{SA}Co_{SA}-Ni₅Co/CNT are shown in **Figure S4**. It can be seen from these figures that the morphologies of Ni_{SA}-Ni/CNT, Ni_{SA}Fe_{SA}-Ni₅Fe/CNT and Ni_{SA}Co_{SA}-Ni₅Co/CNT are similar to that of Ni_{SA}Fe_{SA}-Ni₅₀Fe/CNT. The coating rate on CNT wall and the particle size of nanoalloy are also the same.

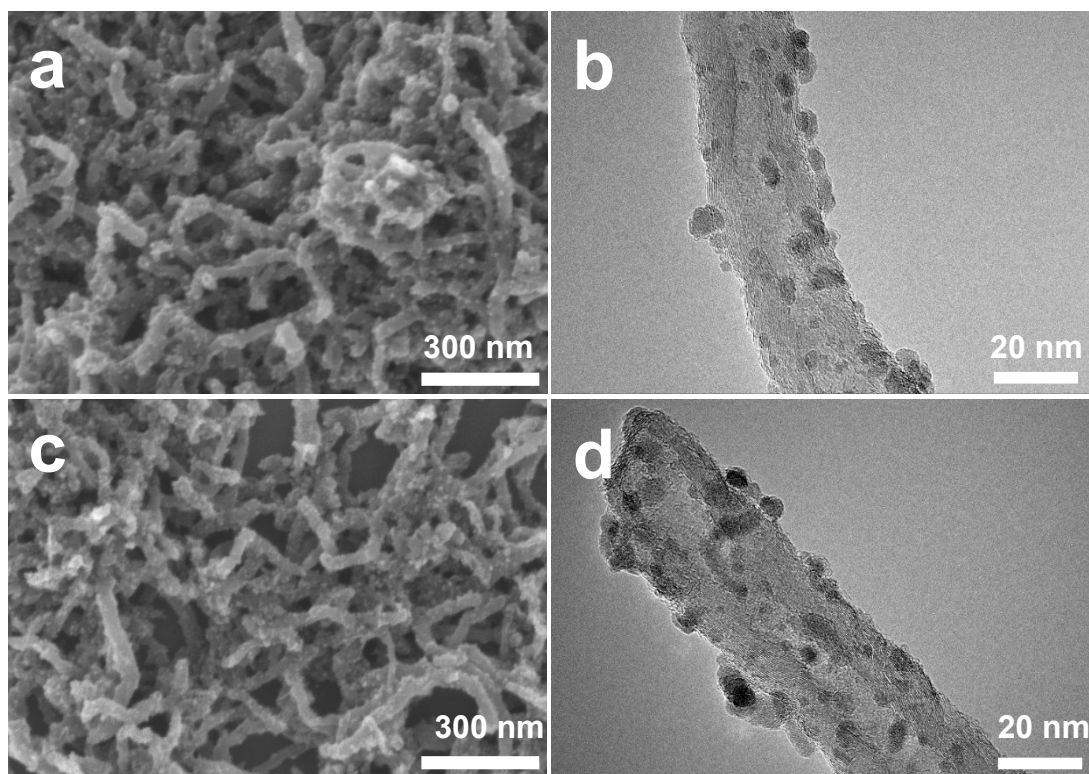


Figure S5. a) SEM image of $\text{Ni}_{\text{SA}}\text{Fe}_{\text{SA}}\text{-Ni}_{10}\text{Fe/CNT}$. b) TEM image of $\text{Ni}_{\text{SA}}\text{Fe}_{\text{SA}}\text{-Ni}_{10}\text{Fe/CNT}$. c) SEM image of $\text{Ni}_{\text{SA}}\text{Co}_{\text{SA}}\text{-Ni}_{50}\text{Co/CNT}$. d) TEM image of $\text{Ni}_{\text{SA}}\text{Co}_{\text{SA}}\text{-Ni}_{50}\text{Co/CNT}$.

The SEM and TEM images of $\text{Ni}_{\text{SA}}\text{Fe}_{\text{SA}}\text{-Ni}_{10}\text{Fe/CNT}$ and $\text{Ni}_{\text{SA}}\text{Co}_{\text{SA}}\text{-Ni}_{50}\text{Co/CNT}$ are shown in **Figure S5**. It can be seen from these figures that the morphologies of $\text{Ni}_{\text{SA}}\text{Fe}_{\text{SA}}\text{-Ni}_{10}\text{Fe/CNT}$ and $\text{Ni}_{\text{SA}}\text{Co}_{\text{SA}}\text{-Ni}_{50}\text{Co/CNT}$ are similar to that of $\text{Ni}_{\text{SA}}\text{Fe}_{\text{SA}}\text{-Ni}_{50}\text{Fe/CNT}$. The coating rate on CNT wall and the particle size of nanoalloy are also the same.

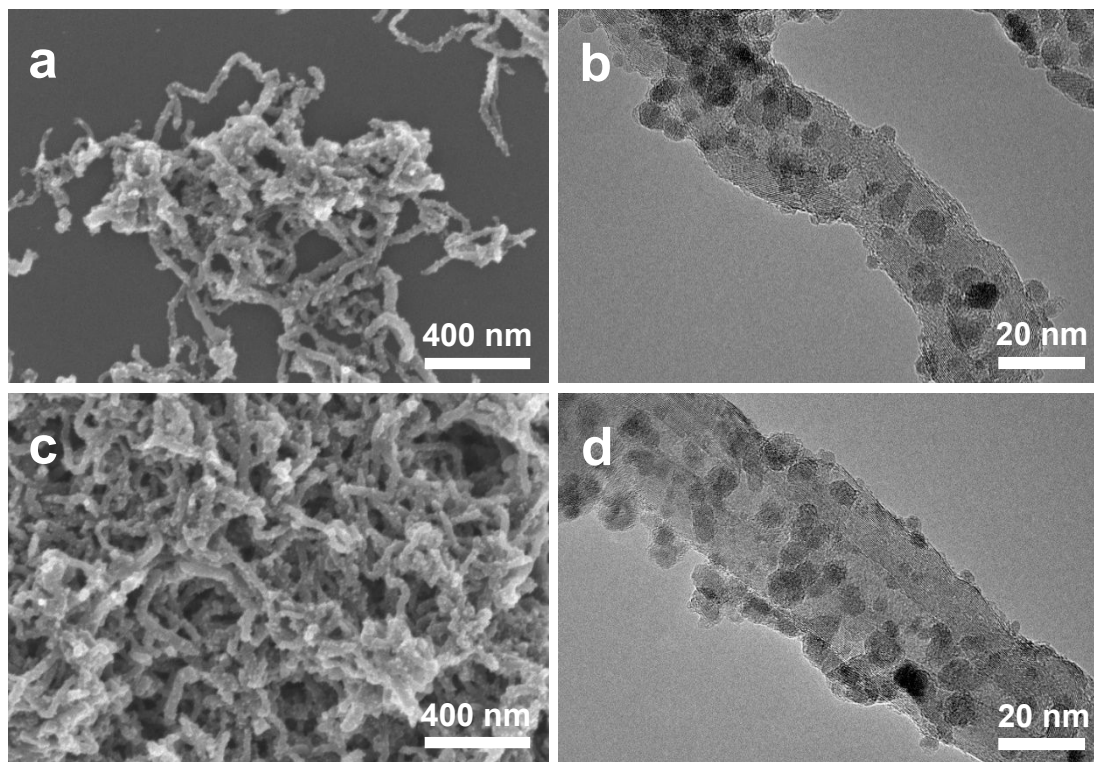


Figure S6. a) SEM image of $\text{Ni}_{\text{SA}}\text{Fe}_{\text{SA}}\text{-Ni}_{30}\text{Fe/CNT}$. b) TEM image of $\text{Ni}_{\text{SA}}\text{Fe}_{\text{SA}}\text{-Ni}_{30}\text{Fe/CNT}$. c) SEM image of $\text{Ni}_{\text{SA}}\text{Co}_{\text{SA}}\text{-Ni}_{30}\text{Co/CNT}$. d) TEM image of $\text{Ni}_{\text{SA}}\text{Co}_{\text{SA}}\text{-Ni}_{30}\text{Co/CNT}$.

The SEM and TEM images of $\text{Ni}_{\text{SA}}\text{Fe}_{\text{SA}}\text{-Ni}_{30}\text{Fe/CNT}$ and $\text{Ni}_{\text{SA}}\text{Co}_{\text{SA}}\text{-Ni}_{30}\text{Co/CNT}$ are shown in **FigureS6**. It can be seen from these figures that the morphologies of $\text{Ni}_{\text{SA}}\text{Fe}_{\text{SA}}\text{-Ni}_{30}\text{Fe/CNT}$ and $\text{Ni}_{\text{SA}}\text{Co}_{\text{SA}}\text{-Ni}_{30}\text{Co/CNT}$ are similar to that of $\text{Ni}_{\text{SA}}\text{Fe}_{\text{SA}}\text{-Ni}_{50}\text{Fe/CNT}$. The coating rate on CNT wall and the particle size of nanoalloy are also the same.

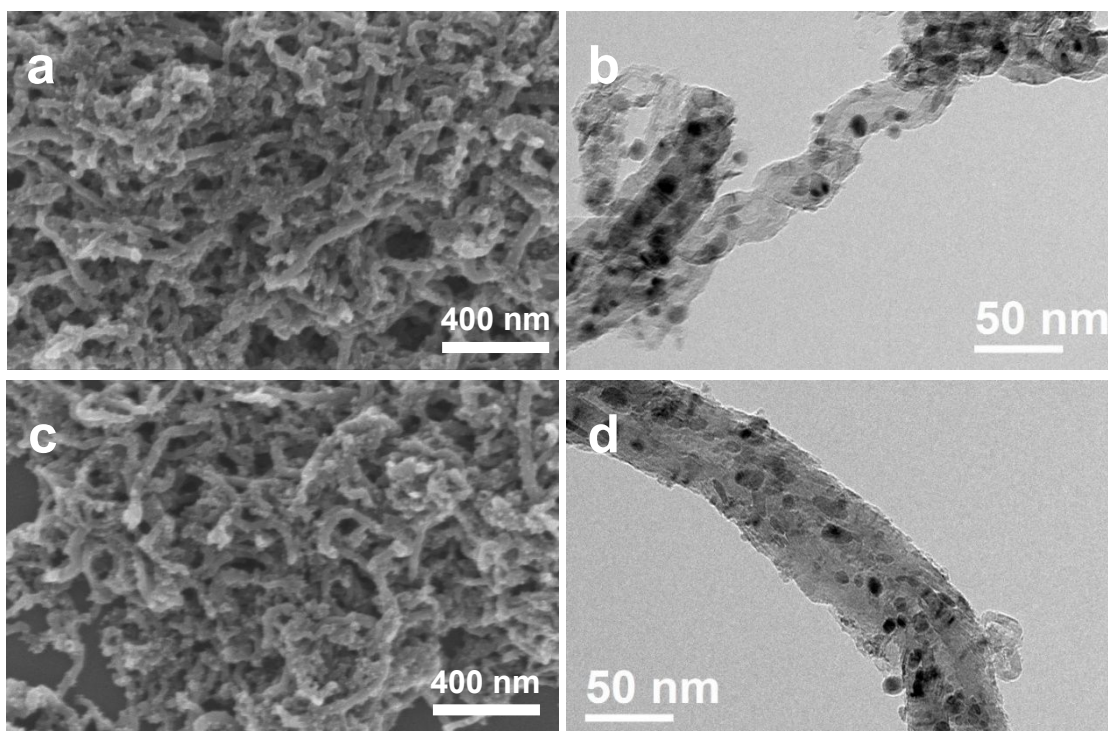


Figure S7. a) SEM image of $\text{Ni}_{\text{SA}}\text{Fe}_{\text{SA}}\text{-Ni}_{70}\text{Fe/CNT}$. b) TEM image of $\text{Ni}_{\text{SA}}\text{Fe}_{\text{SA}}\text{-Ni}_{70}\text{Fe/CNT}$. c) SEM image of $\text{Ni}_{\text{SA}}\text{Co}_{\text{SA}}\text{-Ni}_{70}\text{Co/CNT}$. d) TEM image of $\text{Ni}_{\text{SA}}\text{Co}_{\text{SA}}\text{-Ni}_{70}\text{Co/CNT}$.

The SEM and TEM images of $\text{Ni}_{\text{SA}}\text{Fe}_{\text{SA}}\text{-Ni}_{70}\text{Fe/CNT}$ and $\text{Ni}_{\text{SA}}\text{Co}_{\text{SA}}\text{-Ni}_{70}\text{Co/CNT}$ are shown in **Figure S7**. It can be seen from these figures that the morphologies of $\text{Ni}_{\text{SA}}\text{Fe}_{\text{SA}}\text{-Ni}_{70}\text{Fe/CNT}$ and $\text{Ni}_{\text{SA}}\text{Co}_{\text{SA}}\text{-Ni}_{70}\text{Co/CNT}$ are similar to that of $\text{Ni}_{\text{SA}}\text{Fe}_{\text{SA}}\text{-Ni}_{50}\text{Fe/CNT}$. The coating rate on CNT wall and the particle size of nanoalloy are also the same.

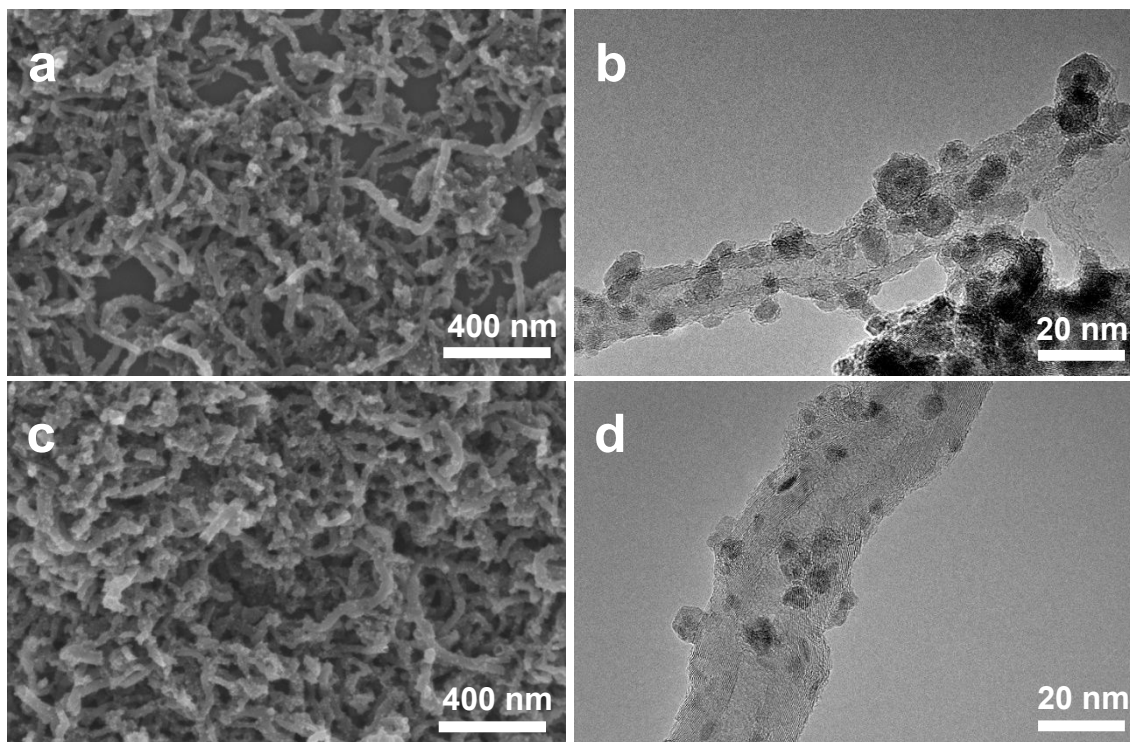


Figure S8. a) SEM image of $\text{Ni}_{\text{SA}}\text{Fe}_{\text{SA}}\text{-Ni}_{100}\text{Fe/CNT}$. b) TEM image of $\text{Ni}_{\text{SA}}\text{Fe}_{\text{SA}}\text{-Ni}_{100}\text{Fe/CNT}$. c) SEM image of $\text{Ni}_{\text{SA}}\text{Co}_{\text{SA}}\text{-Ni}_{100}\text{Co/CNT}$. d) TEM image of $\text{Ni}_{\text{SA}}\text{Co}_{\text{SA}}\text{-Ni}_{100}\text{Co/CNT}$.

The SEM and TEM images of $\text{Ni}_{\text{SA}}\text{Fe}_{\text{SA}}\text{-Ni}_{100}\text{Fe/CNT}$ and $\text{Ni}_{\text{SA}}\text{Co}_{\text{SA}}\text{-Ni}_{100}\text{Co/CNT}$ are shown in **Figure S8**. It can be seen from the figure that the morphologies of $\text{Ni}_{\text{SA}}\text{Fe}_{\text{SA}}\text{-Ni}_{100}\text{Fe/CNT}$ and $\text{Ni}_{\text{SA}}\text{Co}_{\text{SA}}\text{-Ni}_{100}\text{Co/CNT}$ are similar to that of $\text{Ni}_{\text{SA}}\text{Fe}_{\text{SA}}\text{-Ni}_{50}\text{Fe/CNT}$. The coating rate on CNT wall and the particle size of nanoalloy are also the same.

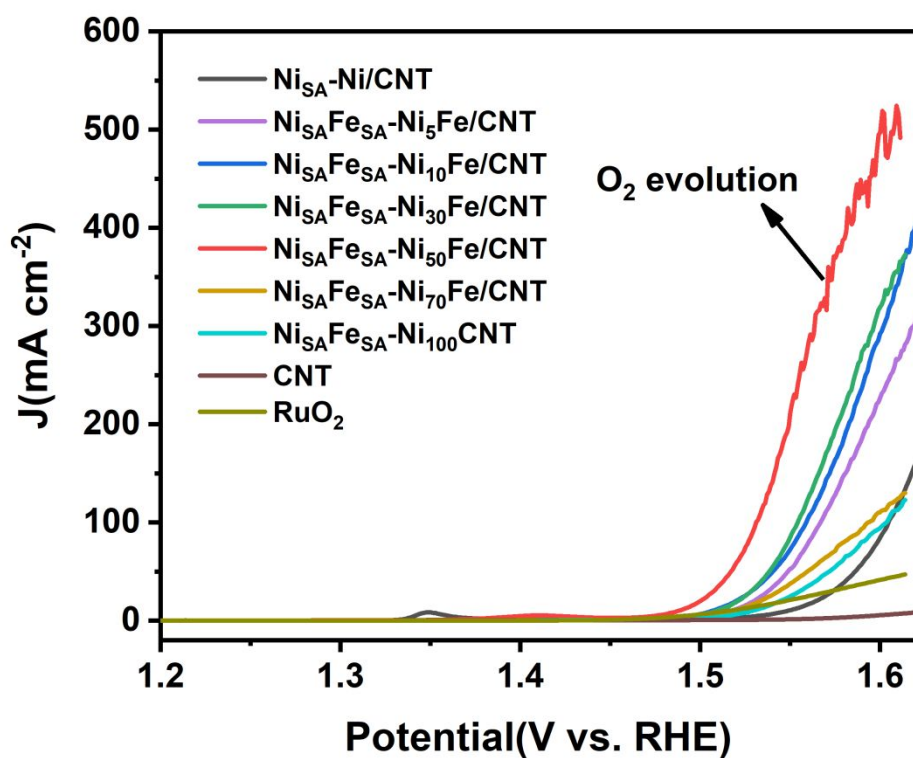


Figure S9. OER performance of $\text{Ni}_{\text{SA}}\text{Fe}_{\text{SA}}\text{-Ni}_x\text{Fe/CNT}$ and RuO_2 loaded on glassy carbon electrode.

Figure S9 shows the OER properties of $\text{Ni}_{\text{SA}}\text{Fe}_{\text{SA}}\text{-Ni}_x\text{Fe/CNT}$ with different proportions of Ni/Fe and RuO_2 loaded on glassy carbon electrode. It can be seen from the figure that the intrinsic OER catalytic performance of $\text{Ni}_{\text{SA}}\text{Fe}_{\text{SA}}\text{-Ni}_{50}\text{Fe/CNT}$ is the best among the $\text{Ni}_{\text{SA}}\text{Fe}_{\text{SA}}\text{-Ni}_x\text{Fe/CNT}$.

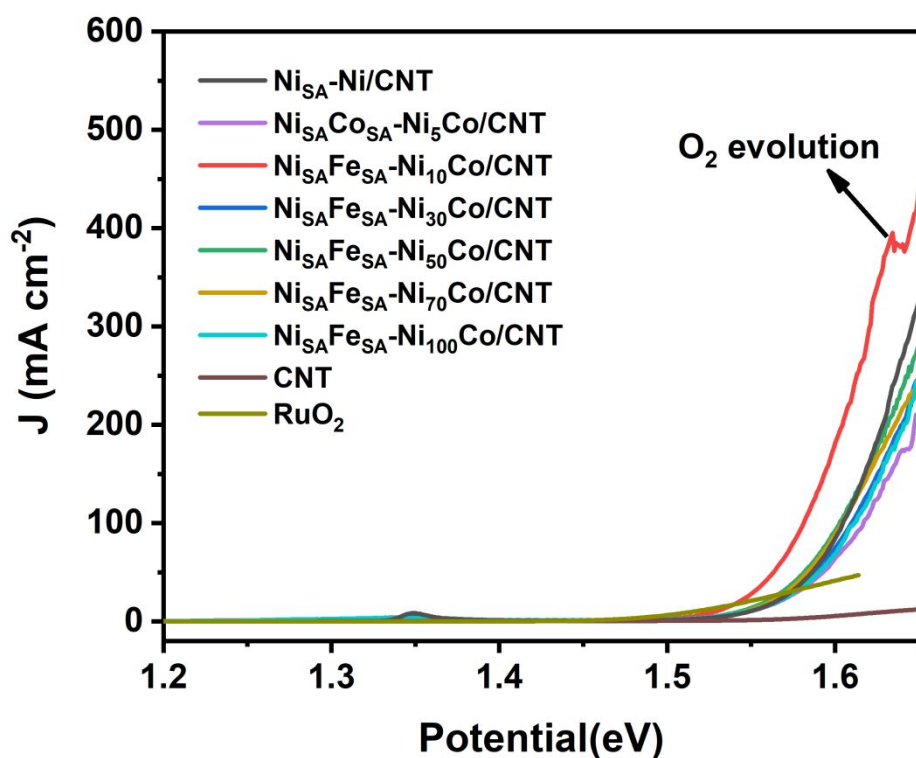


Figure S10. OER performance of $\text{Ni}_{\text{SA}}\text{Co}_{\text{SA}}\text{-Ni}_x\text{Co/CNT}$ loaded on glassy carbon electrode.

Figure S10 shows the OER properties of $\text{Ni}_{\text{SA}}\text{Co}_{\text{SA}}\text{-Ni}_x\text{Co/CNT}$ with different proportions of Ni/Co loaded on glassy carbon electrodes. According to the figure, $\text{Ni}_{\text{SA}}\text{Co}_{\text{SA}}\text{-Ni}_{10}\text{Co/CNT}$ has the best intrinsic OER catalytic performance among $\text{Ni}_{\text{SA}}\text{Co}_{\text{SA}}\text{-Ni}_x\text{Co/CNT}$.

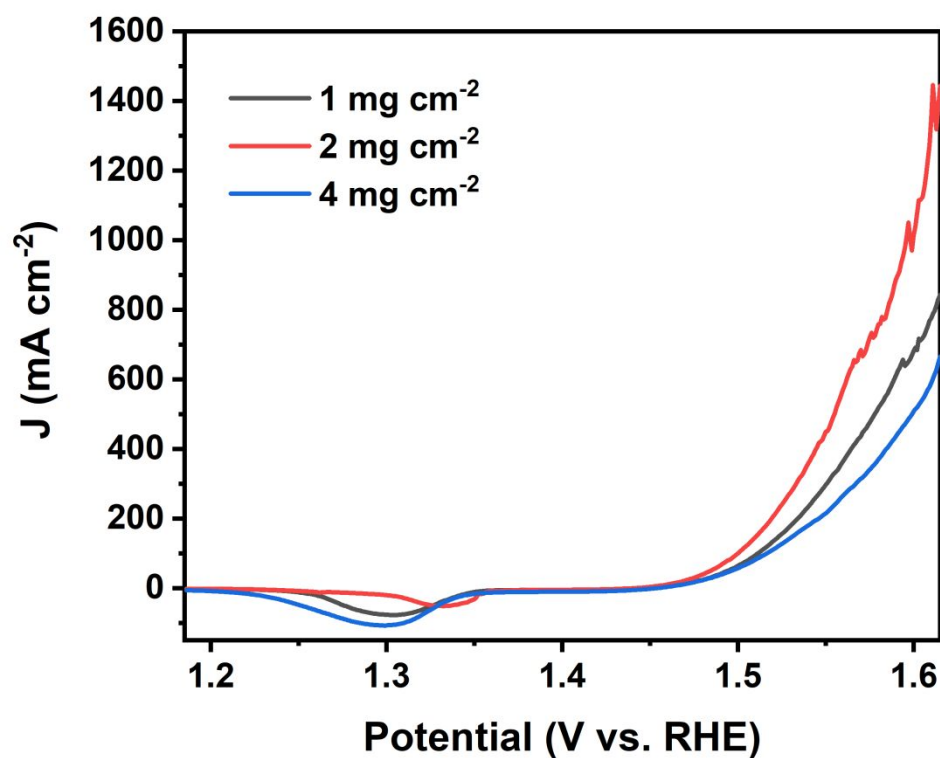


Figure S11. The exploring result of the optimal load for carbon cloth

Figure S11 is the result of the investigation of the optimal loading capacity for $\text{Ni}_{\text{SA}}\text{Fe}_{\text{SA}}\text{-Ni}_{50}\text{Fe/CNT}$ on the carbon cloth. It can be seen from the figure that the optimal loading capacities is 2 mg cm^{-2} .

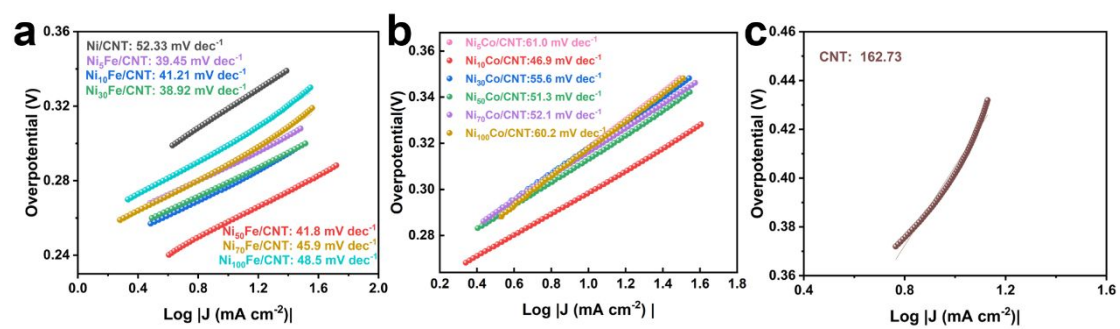


Figure S12. The Tafel slope comparison of Ni_{SA}Fe_{SA}-Ni_xFe/CNT and Ni_{SA}Co_{SA}-Ni_xCo/CNT

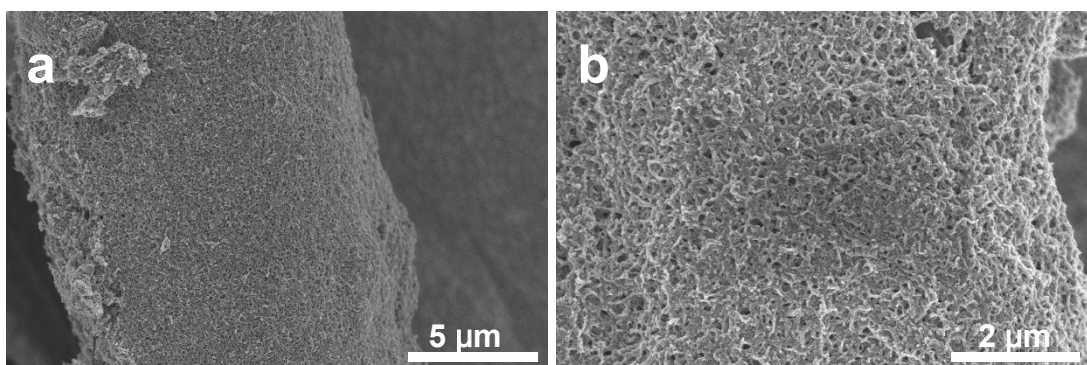


Figure S13. SEM images of $\text{Ni}_{\text{SA}}\text{Fe}_{\text{SA}}\text{-Ni}_{50}\text{Fe/CNT}$ loaded on carbon cloth electrode.

Figure S13 is the SEM images of $\text{Ni}_{\text{SA}}\text{Fe}_{\text{SA}}\text{-Ni}_{50}\text{Fe/CNT}$ loaded on carbon cloth electrode. It can be seen from these figures that $\text{Ni}_{\text{SA}}\text{Fe}_{\text{SA}}\text{-Ni}_{50}\text{Fe/CNT}$ is tightly coated on the carbon fiber. The bonded carbon nanotubes and carbon fibers can be used as electron migration pathways in the catalytic process to improve the kinetic speed of the catalyst.

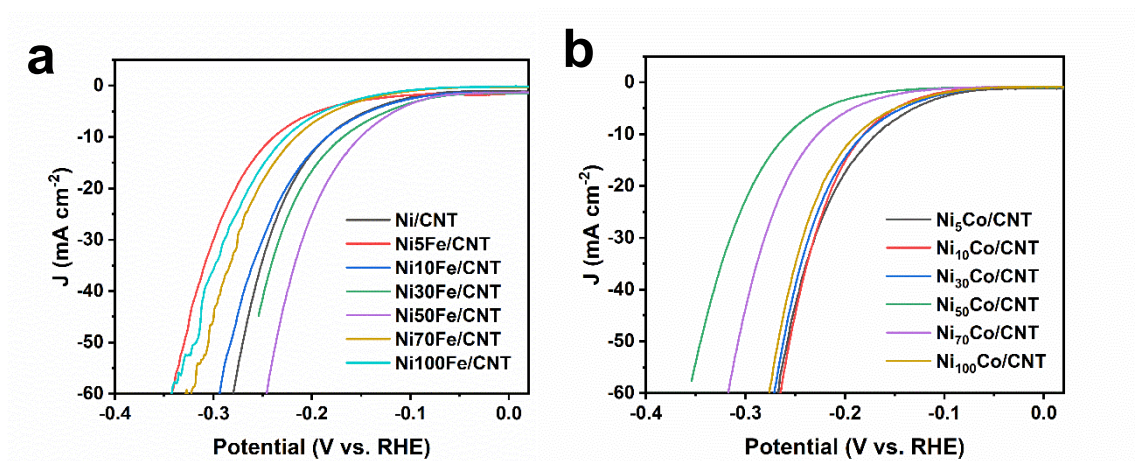


Figure S14. HER properties of $\text{Ni}_{\text{SA}}\text{Fe}_{\text{SA}}\text{-Ni}_x\text{Fe/CNT}$ and $\text{Ni}_{\text{SA}}\text{Co}_{\text{SA}}\text{-Ni}_x\text{Co/CNT}$ loaded on glassy carbon electrode.

Figure S14 shows the HER properties of $\text{Ni}_{\text{SA}}\text{Fe}_{\text{SA}}\text{-Ni}_x\text{Fe/CNT}$ and $\text{Ni}_{\text{SA}}\text{Co}_{\text{SA}}\text{-Ni}_x\text{Co/CNT}$ with different proportions of Ni/Fe and Ni/Co loaded on glassy carbon electrodes. It can be seen from these figures that $\text{Ni}_{\text{SA}}\text{Fe}_{\text{SA}}\text{-Ni}_{50}\text{Fe/CNT}$ has the best intrinsic HER catalytic performance among $\text{Ni}_{\text{SA}}\text{Fe}_{\text{SA}}\text{-Ni}_x\text{Fe/CNT}$, and $\text{Ni}_{\text{SA}}\text{Co}_{\text{SA}}\text{-Ni}_5\text{Co/CNT}$ has the best intrinsic HER catalytic performance among $\text{Ni}_{\text{SA}}\text{Co}_{\text{SA}}\text{-Ni}_x\text{Co/CNT}$.

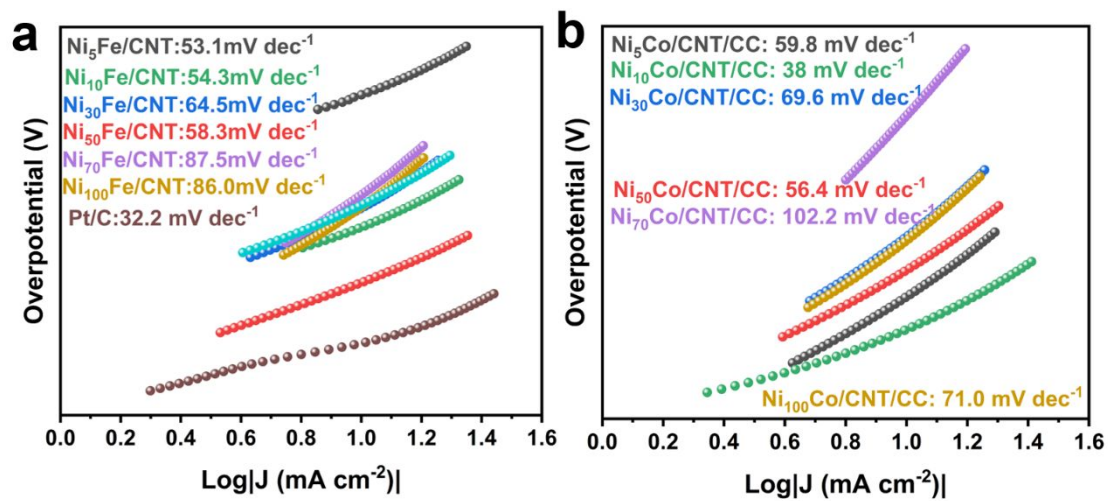


Figure S15. The Tafel slope comparison of Ni_{SA}Fe_{SA}-Ni_xFe/CNT and Ni_{SA}Co_{SA}-Ni_xCo/CNT

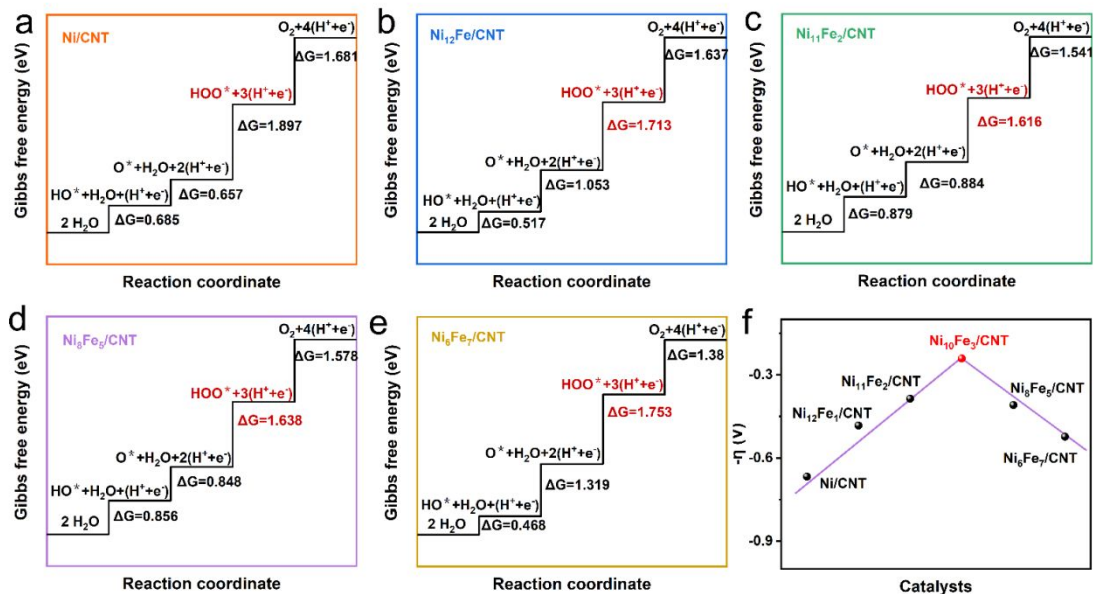


Figure S16. Schematic diagram of free energy model of Ni_xFe_y/CNT in different proportions and volcanic pattern diagram of overpotential a) Ni/CNT. b) Ni₁₂Fe/CNT. c) Ni₁₁Fe₂/CNT. d) Ni₈Fe₅/CNT. e) Ni₆Fe₇/CNT. f) Overpotential volcanic patterns of Ni/CNT, Ni₁₂Fe/CNT, Ni₁₁Fe₂/CNT, Ni₁₀Fe₃/CNT, Ni₈Fe₅/CNT and Ni₆Fe₇/CNT

The free energies of Ni/CNT, Ni₁₂Fe/CNT, Ni₁₁Fe₂/CNT, Ni₈Fe₅/CNT and Ni₆Fe₇/CNT are shown in **Figure S16a-e**. It can be seen from these figures that the rate-determining step of Ni/CNT, Ni₁₂Fe/CNT, Ni₁₁Fe₂/CNT, Ni₈Fe₅/CNT and Ni₆Fe₇/CNT is the third step. Figure S14f shows the volcanic pattern for overpotentials of Ni/CNT, Ni₁₂Fe/CNT, Ni₁₁Fe₂/CNT, Ni₈Fe₅/CNT and Ni₆Fe₇/CNT. It can be seen from the figure that the overpotential of Ni₁₀Fe₃/CNT is the lowest.

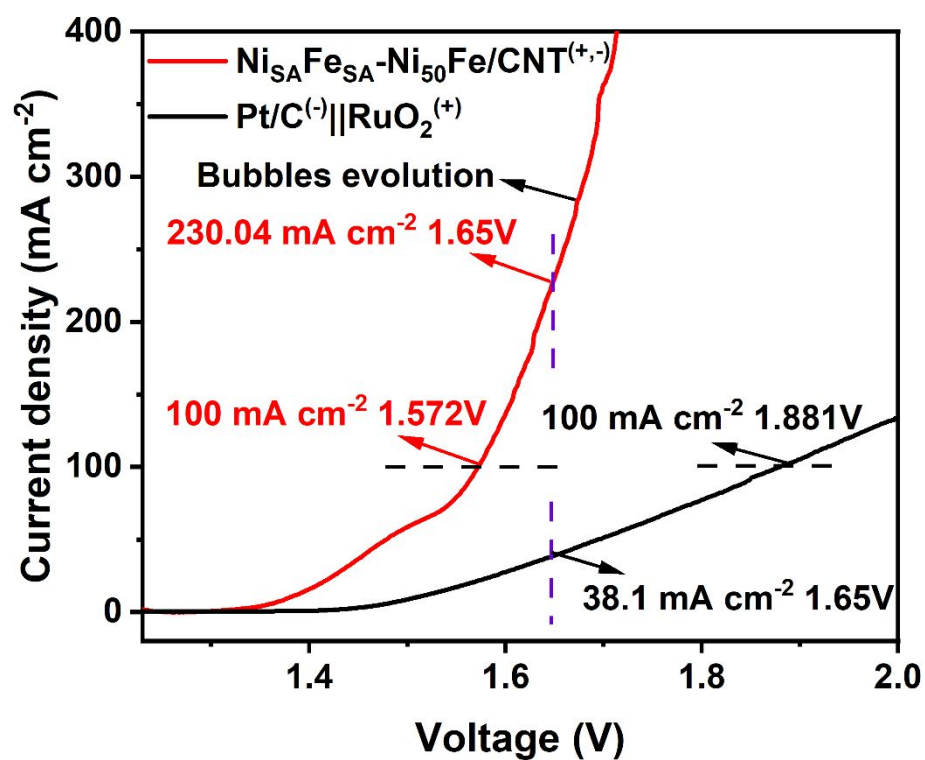


Figure S17. The LSV curves of $\text{Ni}_{\text{SA}}\text{Fe}_{\text{SA}}\text{-Ni}_{50}\text{Fe/CNT}^{(+,-)}$ electrolyzer with positive scanning (from low voltage to high voltage)

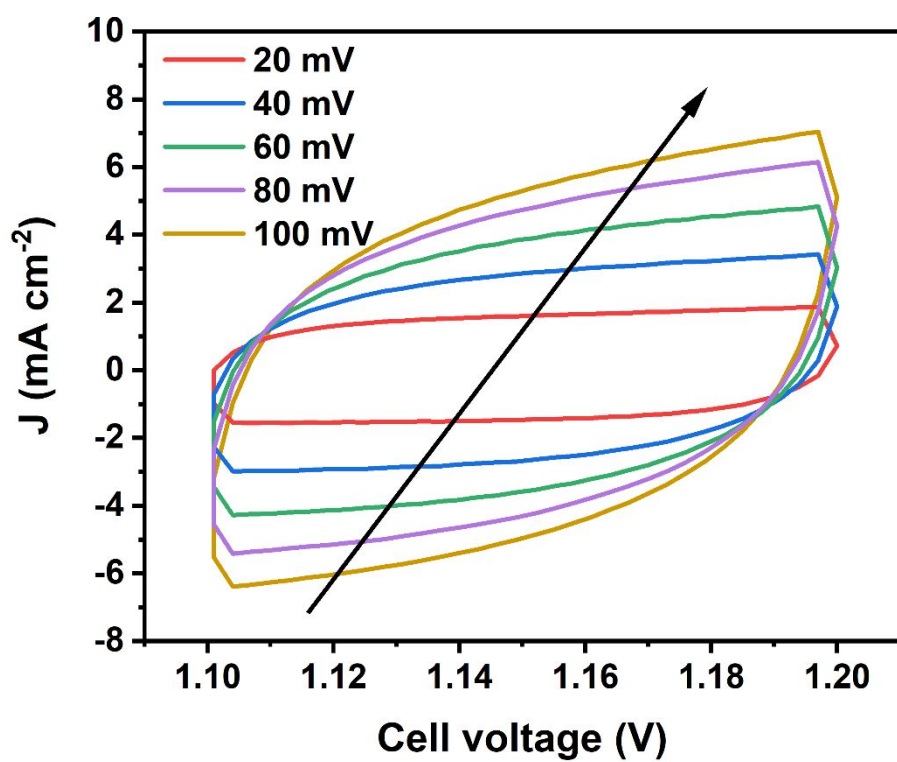


Figure S18. The CV curves of $\text{Ni}_{\text{SA}}\text{Fe}_{\text{SA}}\text{-Ni}_{50}\text{Fe/CNT}^{(+,-)}$ electrolyzer at the scan rate of 20, 40, 60, 80 and 100 mV s^{-1}

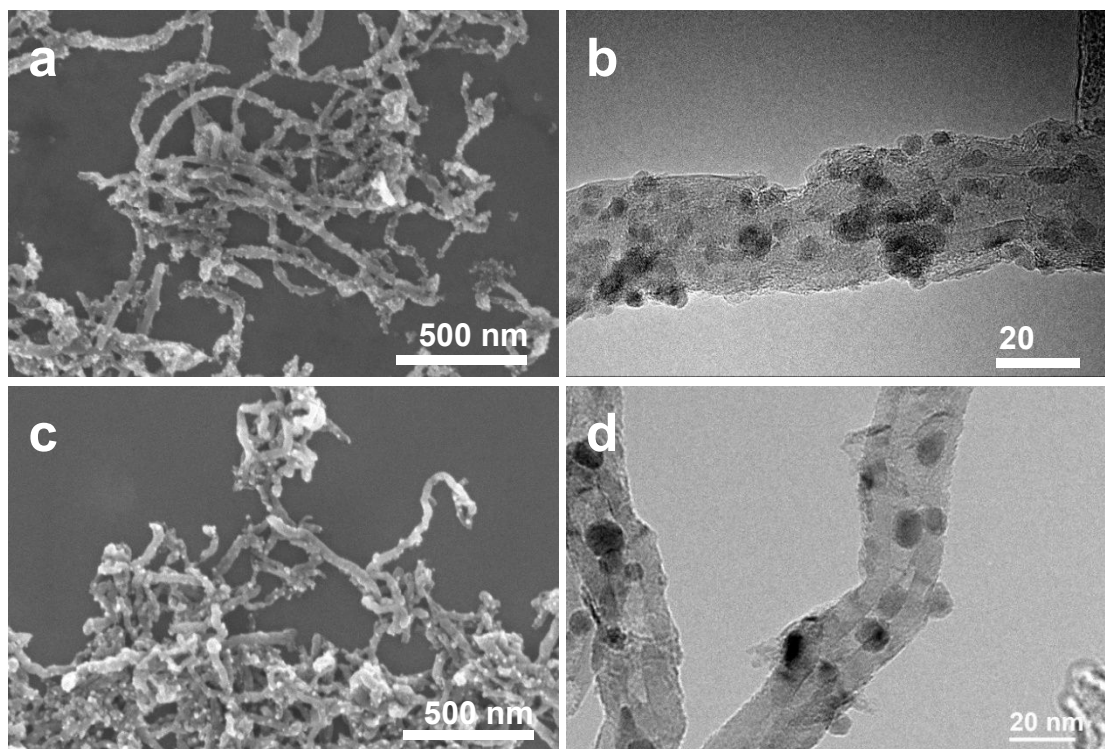


Figure S19. Morphologies of oxidized and re-reduced $\text{Ni}_{\text{SA}}\text{Fe}_{\text{SA}}\text{-Ni}_{50}\text{Fe/CNT}$. a, b) SEM and TEM image of oxidized $\text{Ni}_{\text{SA}}\text{Fe}_{\text{SA}}\text{-Ni}_{50}\text{Fe/CNT}$. c, d) SEM and TEM images of $\text{Ni}_{\text{SA}}\text{Fe}_{\text{SA}}\text{-Ni}_{50}\text{Fe/CNT}$ after re-reduction.

It can be seen from these figures that the morphologies of the oxidized and re-reduced $\text{Ni}_{\text{SA}}\text{Fe}_{\text{SA}}\text{-Ni}_{50}\text{Fe/CNT}$ has no obvious change compared with the original one.

Supplementary Table S1. EXAFS fitting parameters at the Fe and Ni K-edge for various samples.

Sample	Shell	CN^a	$R(\text{\AA})^b$	$\sigma^2(\text{\AA}^2)^c$	$\Delta E_0(\text{eV})_d$	R factor
Fe K-edge ($S_0^2=0.703$)						
Fe foil	Fe-Fe	8*	2.47±0.01	0.0048±0.0003	7.4±1.2	0.0020
	Fe-Fe	6*	2.85±0.01	0.0066±0.0009		
Fe in Ni _{SA} Fe _{SA} - Ni ₅₀ Fe/C NT	Fe-O	1.7±0.6	2.07±0.01	0.0069±0.0006	5.2±8.8	0.0073
	Fe- Fe/Ni	3.6±0.3	2.68±0.01	0.0057±0.0016		
Ni K-edge ($S_0^2=0.824$)						
Ni foil	Ni-Ni	12*	2.48±0.01	0.0061±0.0003	7.2±0.4	0.0018
Ni in Ni _{SA} Fe _{SA} - Ni ₅₀ Fe/C NT	Ni-O	3.2±1.0	2.08±0.01	0.0025±0.0001	2.9±2.5	0.0152
	Ni- Ni/Fe	9.6±3.2	2.54±0.02	0.0105±0.0034		

^a CN , coordination number; ^b R , distance between absorber and backscatter atoms; ^c σ^2 , Debye-Waller factor to account for both thermal and structural disorders; ^d ΔE_0 , inner potential correction; R factor indicates the goodness of the fit. S_0^2 was fixed to 0.703 and 0.824, according to the experimental EXAFS fit of Fe foil and Ni foil by fixing CN as the known crystallographic value. Fitting range: $3.0 \leq k (\text{\AA}) \leq 12.4$ and $1.0 \leq R (\text{\AA}) \leq 3.0$ (Fe foil and Ni foil); $2.0 \leq k (\text{\AA}) \leq 9.0$ and $1.0 \leq R (\text{\AA}) \leq 3.0$ (Fe); $2.0 \leq k (\text{\AA}) \leq 10.0$ and $1.1 \leq R (\text{\AA}) \leq 3.0$ (Ni). A reasonable range of EXAFS fitting parameters: $0.700 < S_0^2 < 1.000$; $CN > 0$; $\sigma^2 > 0 \text{\AA}^2$; $\Delta E_0 < 10 \text{ eV}$; $R \text{ factor} < 0.02$.

Supplementary Table S2. Comparison of the overall-water-splitting activities among different earth-abundant electrocatalysts tested in 1 M KOH. η_{10} , η_{100} and η_{400} correspond to the overpotentials of the overall water splitting cell operated at 10, 100, and 400 mA cm⁻², respectively. $J_{1.615\text{ V}}$ represents the current density at a cell voltage of 1.615 V.

Electrolyzers	η_{10} [mV]	η_{100} [mV]	η_{400} [mV]	$J_{1.615\text{ V}}$ [mA cm ⁻²]	Reference
Ni _{SA} Fe _{SA} -Ni ₅₀ Fe/CNT (+, -)	150	342	481	162	Our work
Ni-Fe NP (+, -)	240	525*	NA	14*	Nature Communication, 2019(10):5599 ¹
Cu@NiFe LDH (+, -)	310	460	NA	48*	Energy & Environmental Science, 2017(10): 1820-1827 ²
Co-NC@CC (+, -)	340	NA	NA	12*	Advanced Functional Materials, 2021, 2009853 ³
Co, Nb-MoS ₂ /TiO ₂ HSs (+, -)	360	914*	NA	12*	Nano Energy 82 (2021) 105750 ⁴
FeNi@N-CNT (+, -)	370	845*	NA	13*	ACS Applied Materials & Interfaces, 2016(8) 35390–35397 ⁵
NiFe-PVP NiMo- PVP	430	NA	NA	5*	Advanced Energy Materials, 2017, 1700220 ⁶
Ni ₂ Fe ₁ -O (+, -)	430	NA	NA	7*	Advanced Energy Materials, 2017, 1701347 ⁷
FeCo-FeCoNi (+, -)	457	NA	NA	3*	ACS Catalysis, 2017(7) 469–479 ⁸

* The value is calculated from the curves shown in the literature.

REFERENCES

- (1) Suryanto, B. H. R.; Wang, Y.; Hocking, R. K.; Adamson, W.; Zhao, C., Overall electrochemical splitting of water at the heterogeneous interface of nickel and iron oxide. *Nat. Commun.* **2019**, 10 (1), 5599.
- (2) Yu, L.; Zhou, H.; Sun, J.; Qin, F.; Yu, F.; Bao, J.; Yu, Y.; Chen, S.; Ren, Z., Cu nanowires shelled with NiFe layered double hydroxide nanosheets as bifunctional electrocatalysts for overall water splitting. *Energy Environ. Sci.* **2017**, 10 (8), 1820-1827.
- (3) Zhong, Y.; Lu, Y.; Pan, Z.; Yang, J.; Du, G.; Chen, J.; Zhang, Q.; Zhou, H.; Wang, J.; Wang, C.; Li, W., Efficient Water Splitting System Enabled by Multifunctional Platinum-Free Electrocatalysts. *Adv. Funct. Mater.* **2021**, 31 (20), e2009853.
- (4) Nguyen, D. C.; Luyen Doan, T. L.; Prabhakaran, S.; Tran, D. T.; Kim, D. H.; Lee, J. H.; Kim, N. H., Hierarchical Co and Nb dual-doped MoS₂ nanosheets shelled micro-TiO₂ hollow spheres as effective multifunctional electrocatalysts for HER, OER, and ORR. *Nano Energy* **2021**, 82, 105750.
- (5) Tao, Z.; Wang, T.; Wang, X.; Zheng, J.; Li, X., MOF-Derived Noble Metal Free Catalysts for Electrochemical Water Splitting. *ACS Appl Mater Interfaces* **2016**, 8 (51), 35390-35397.

- (6) Zhang, Y.; Xia, X.; Cao, X.; Zhang, B.; Tiep, N. H.; He, H.; Chen, S.; Huang, Y.; Fan, H. J., Ultrafine Metal Nanoparticles/N-Doped Porous Carbon Hybrids Coated on Carbon Fibers as Flexible and Binder-Free Water Splitting Catalysts. *Adv. Energy Mater.* **2017**, 7 (15), e1700220.
- (7) Dong, C.; Kou, T.; Gao, H.; Peng, Z.; Zhang, Z., Eutectic-Derived Mesoporous Ni-Fe-O Nanowire Network Catalyzing Oxygen Evolution and Overall Water Splitting. *Adv. Energy Mater.* **2018**, 8 (5), e1701347.
- (8) Yang, Y.; Lin, Z.; Gao, S.; Su, J.; Lun, Z.; Xia, G.; Chen, J.; Zhang, R.; Chen, Q., Tuning Electronic Structures of Nonprecious Ternary Alloys Encapsulated in Graphene Layers for Optimizing Overall Water Splitting Activity. *ACS Catal.* **2016**, 7 (1), 469-479.